Draft compiled: November 3, 2021

Supporting information

1. Dynamic similarity

Given that the aim of this study is to provide insight into flow–transport–morphology feedbacks for protodunes in the field, it is important to consider the dynamic similarity of the laboratory flow environment with that of the atmospheric surface layer. First, it should be understood that although protodunes in the field are wind-driven, and the models in the lab are immersed in a liquid, the difference in the working fluid is not responsible for any difference in the flow physics. The flume has no mobile sediment grains in the flow, only the solid, wall-attached protodune model, and therefore the fluid medium (i.e., gas or liquid) and the differences in their density are not important. Instead, to establish dynamic similarity between the flume and the field, in terms of the flow, the following must be addressed: 1) the large disparity in Re between the laboratory-scale experiment and the atmospheric surface layer (ASL), and 2) the scaling of the protodune within the boundary layer.

In the atmospheric surface layer, the flow is typically characterized by an extremely high Re, $Re_\tau \sim \mathrm{O}(10^6)$ (Hutchins et al., 2012; Wang and Zheng, 2016), three orders of magnitude greater than what can be achieved in the laboratory setting used herein. This disparity is reconciled, however, in the so-called “log layer” of the boundary layer, where the inner and outer regions overlap and exhibit a logarithmic mean velocity profile when scaled in viscous “wall” units (i.e., normalized with $u_\star$ and ν). This log layer is a universal feature of wall-bounded turbulence, and, moreover, the dynamics of the flow in this region, as well as its turbulence statistics, exhibit Re similarity (Marusic et al., 2013). The ASL has been characterized in this regard by Hutchins et al. (2012), who note that, under nearly-neutral stratified conditions, the log layer of the ASL follows the behavior of laboratory-scale boundary layers. This includes coherent structures such as hairpin vortices, ramp-like structures, large-scale mo-

tions (LSMs), and very-large-scale motions (VLSMs) (also called “superstructures”), which have been documented in the ASL (e.g., Hommema and Adrian, 2003; Morris et al., 2007; Chauhan et al., 2013). A necessary condition is that the flow Re must be sufficiently high in the laboratory environment such that a substantial logarithmic region is developed (as Reynolds number increases, the log layer thickens), which is met by the $Re_\tau = 1600$ boundary layer studied herein. Therefore, in terms of the incoming flow, the immersion of the protodune within the log layer means that it is exposed to a flow field that is dynamically similar to that of the atmospheric surface layer under near-neutral stratification.

The second issue, that of the scaling of the protodune within the boundary layer, is more challenging and requires careful consideration for correct interpretation of the results presented herein. While still a topic of active research, Townsend’s attached eddy hypothesis (Townsend, 1976; Marusic and Monty, 2019) implies that in the log layer, the size of turbulent eddies exhibit a linear growth and thus, being “attached”, scale with distance from the wall. This self-similarity exists across a broad range of scales, and involves a constant aspect ratio of the hierarchies of eddies in the log layer (Del Álamo et al., 2006; Baars et al., 2017; Krug et al., 2019). Baars et al. (2017) give an aspect ratio of $\lambda_x/z \approx 14$, with an upper bound for this scaling at $\lambda_x/\delta \approx 10$, where λ_x is the streamwise wavelength of the eddies. This self-similarity was likewise shown for the spanwise dimension by Krug et al. (2019) in the ASL, while linear scaling of spanwise coherence was also shown in laboratory boundary layers by Tomkins and Adrian (2003), Ganapathisubramani et al. (2005), and Hutchins et al. (2005). Furthermore, Salesky and Anderson (2018) have shown that the convective boundary layer remains similar to the stably stratified condition in terms of the existence and self-similarity of LSM and VLSM, including their modulating influence on near-wall turbulence. Thus the immersion of a protodune model within the log layer should mean that the scaling relationship between turbulent eddies and the protodune within the flume is self-similar to that encountered in the field.

Table 1: PIV details

	Measurement plane		
	x–*z*	*x*–*y*	*y*–*z*
Camera	TSI 29MP	TSI 29MP	Phantom v641
Sensor size	6600×4400 pixels^2	6600×4400 pixels^2	2560×1600 pixels^2
Laser	Quantel Evergreen	Quantel Evergreen	NG Patara
Max pulse energy	200 mJ	200 mJ	50 mJ
Tracer particles	Ag-coated solid PMMA	Ag-coated solid PMMA	Ag-coated hollow glass
Tracer size	11 μm	11 μm	14 μm
Sampling rate	0.58 Hz	0.58 Hz	20 Hz
Ensemble size	5000	5000	10,936
Final PIV spot size	16 pixels^2	16 pixels^2	16 pixels^2
Vector grid spacing	350 μm	350 μm	336 μm

2. Details of particle image velocimetry

For the flow-parallel *x*–*z* and *x*–*y* planes, a single TSI 29MP CCD camera was used with a 100 mm Tokina lens. Silver-coated, solid PMMA spheres 11 μm in diameter were used as seeding particles, which were illuminated using a dual-cavity, Quantel Evergreen 532 nm Nd:YAG laser capable of 200 mJ per pulse. The laser beam was collimated and spread into a 2D sheet with a series of spherical and cylindrical lenses, with the thickness of the sheet measuring ≈ 0.5 mm thick and ≈ 1 mm thick in the *x*–*z* and *x*–*y* planes, respectively, with the latter being limited by the distance over which the laser beam required collimation. For both flow-parallel planes, 5000 image pairs were acquired at 0.58 Hz, while the cross-stream data were collected at 20 Hz using a dual-cavity, Northrop Grumman Nd:YLF laser capable of 50 mJ per pulse. In all cases, however, these acquisition rates were low enough that consecutive velocity fields were statistically independent.

3. Coordinates, variables, and other nomenclature

In the following, U, V, and W refer to the instantaneous (i.e., non-fluctuating) velocity components in x, y, and z, respectively. Variables u, v, and w refer to fluctuating velocity components (e.g., $u = U - \langle U \rangle$), where brackets $\langle \cdot \rangle$ indicate temporal averaging over data ensemble and overbar $\bar{\cdot}$ indicates spatial averaging. The subscript "ref" indicates reference data taken from the same dataset but from the farthest available upstream location (i.e., unperturbed) within the field-of-view (FOV). The coordinate z_s refers to distance above the surface in the z-direction.

To capture the turbulent fluxes of momentum across and parallel to streamlines, which are nearly parallel to the underlying surface on the stoss side, most of the data presented herein are analyzed using streamline-corrected coordinates. This approach maintains consistency with typical field data presentation (Wiggs et al., 1996; Claudin et al., 2013), as well as laboratory studies of flow over "gentle bumps" (e.g., Finnigan et al., 1990). Variables with an asterisk (e.g., V^*) indicate that they have not had any coordinate system transformation applied, in which streamwise coordinates are made to be parallel to the local streamlines. As most of the results in the following involve this pre-processing step, variables without an asterisk indicate streamline-corrected data. The coordinate system transformation is applied to the instantaneous velocity fields for the data in the x–z plane following

$$\theta_{xz}(x,z) = \tan\left(\frac{\langle W^*(x,z)\rangle}{\langle U^*(x,z)\rangle}\right)^{-1} \tag{1}$$

$$U = U^*\cos(\theta_{xz}) + W^*\sin(\theta_{xz}) \tag{2}$$

$$W = -U^*\sin(\theta_{xz}) + W^*\cos(\theta_{xz}), \tag{3}$$

and similarly for the x–y plane as

$$\theta_{xy}(x,y) = \tan\left(\frac{\langle V^*(x,y)\rangle}{\langle U^*(x,y)\rangle}\right)^{-1} \tag{4}$$

$$U = U^* \cos(\theta_{xy}) + V^* \sin(\theta_{xy}) \tag{5}$$

$$V = -U^* \sin(\theta_{xy}) + V^* \cos(\theta_{xy}). \tag{6}$$

In the y–z plane, where all three velocity components are measured simultaneously, the transformation for x–y is applied first, followed by the x–z transformation.

4. Mean velocities

Perturbations of W^* are shown in Fig. 1, where the normalized disparities are on the order of 10% of the free stream velocity. It must be noted that the normalization of the disparity here is different from that used for $\langle U \rangle$, as $\langle W^* \rangle$ is zero in the incoming flow and thus unsuitable for use in normalization. In all cases, the flow is diverted upward beginning just after the toe and up until the crest is reached, after which the flow directed downward in the lee. The strength of the topographic forcing is compared in profiles from $z_s/H = 0.2$ in Fig. 2, including the Mature case.

The lateral steering of the mean flow is shown in Fig. 3 where, similar to W^*, the values are on the order of 5% of the free stream velocity. Here also the trends and symmetry are clearly quite consistent across all cases, as flow diverts outward (away from the centerline) on the stoss side, and then inward beyond the crest.

Although only collected for the CrestMidA case, data from the y-z plane further elucidate the three-dimensionality of the mean velocity changes. It can be seen that acceleration of flow over the crest extends out in the span as well, above the surface, until the flat wall is reached. This layer of acceleration flow grows gradually thinner, but remains relatively high. Due to the flat crest, changes in $\langle W^* \rangle$ are relatively small near the centerline, but are maximal around

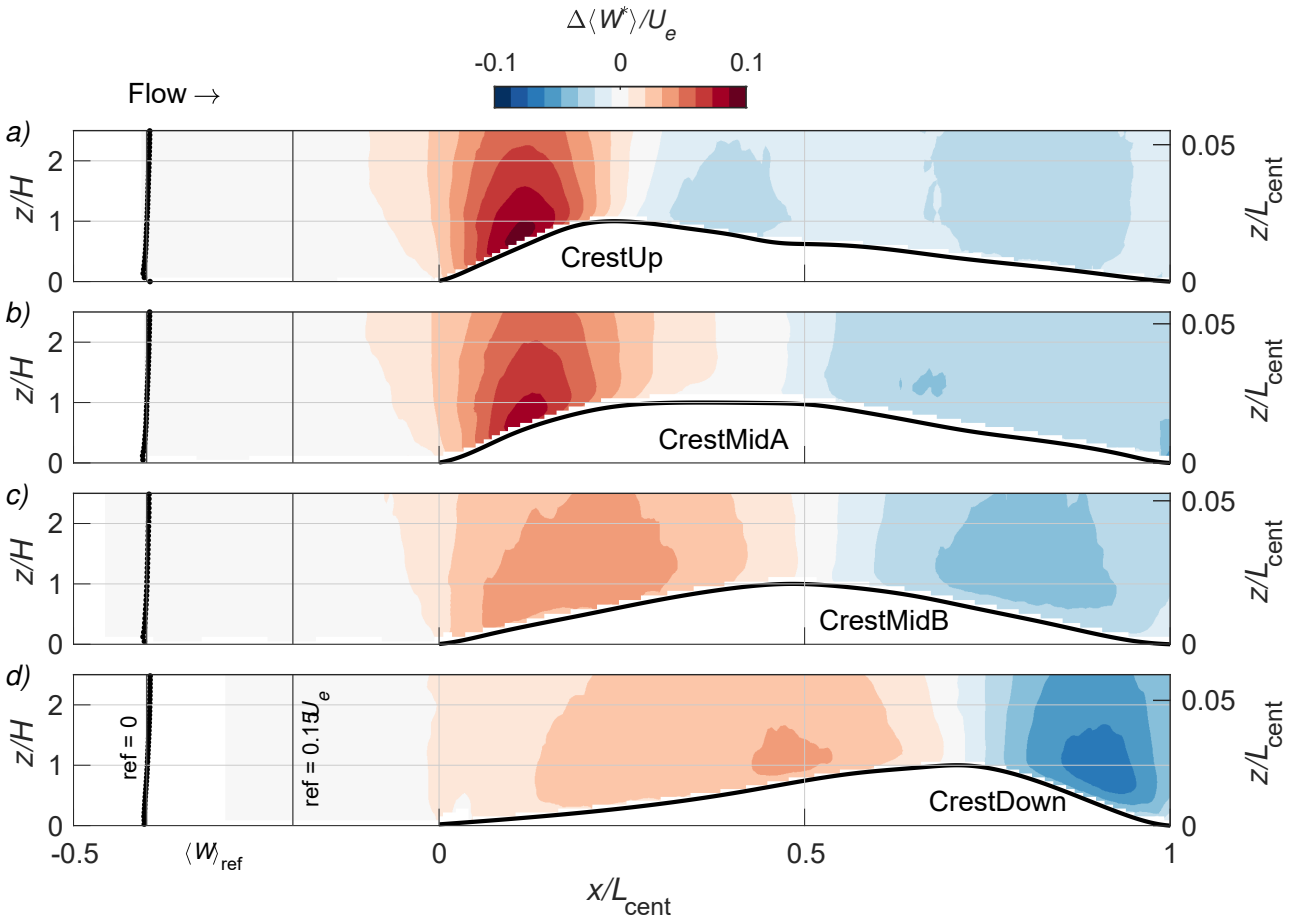

Figure 1: Disparity maps of $\langle W^* \rangle$ along x–z centerline plane (y=0). Dotted profile overlaid upstream shows reference data used for calculating disparity.

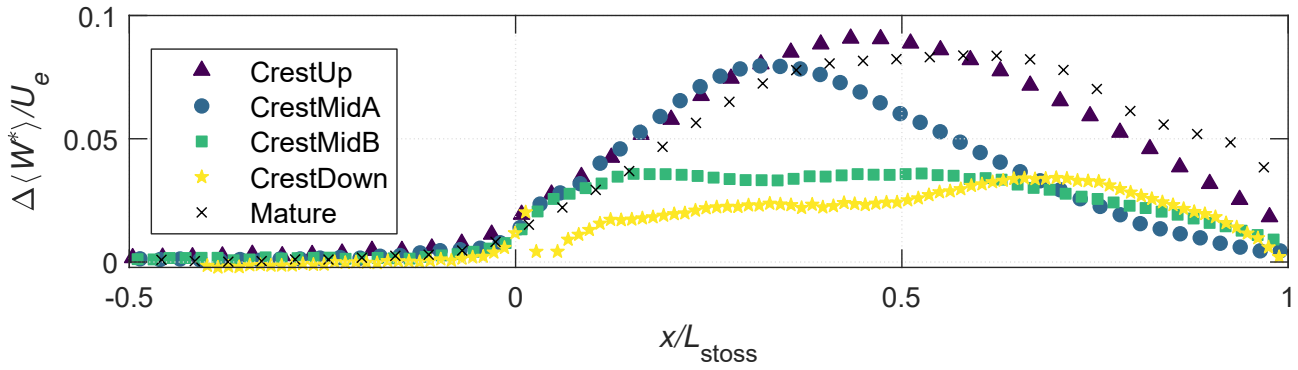

Figure 2: Constant elevation profiles of mean vertical velocity from the x–z centerline plane plotting data from $z_s/H = 0.2$. L_{stoss} is the x-distance from toe to crest.

$y/L_y = 0.25$, which is where the convex surface curvature is highest. Lateral steering of the flow, meanwhile, is strongest where the topography meets the wall, around $y/L_y = 0.4$. This

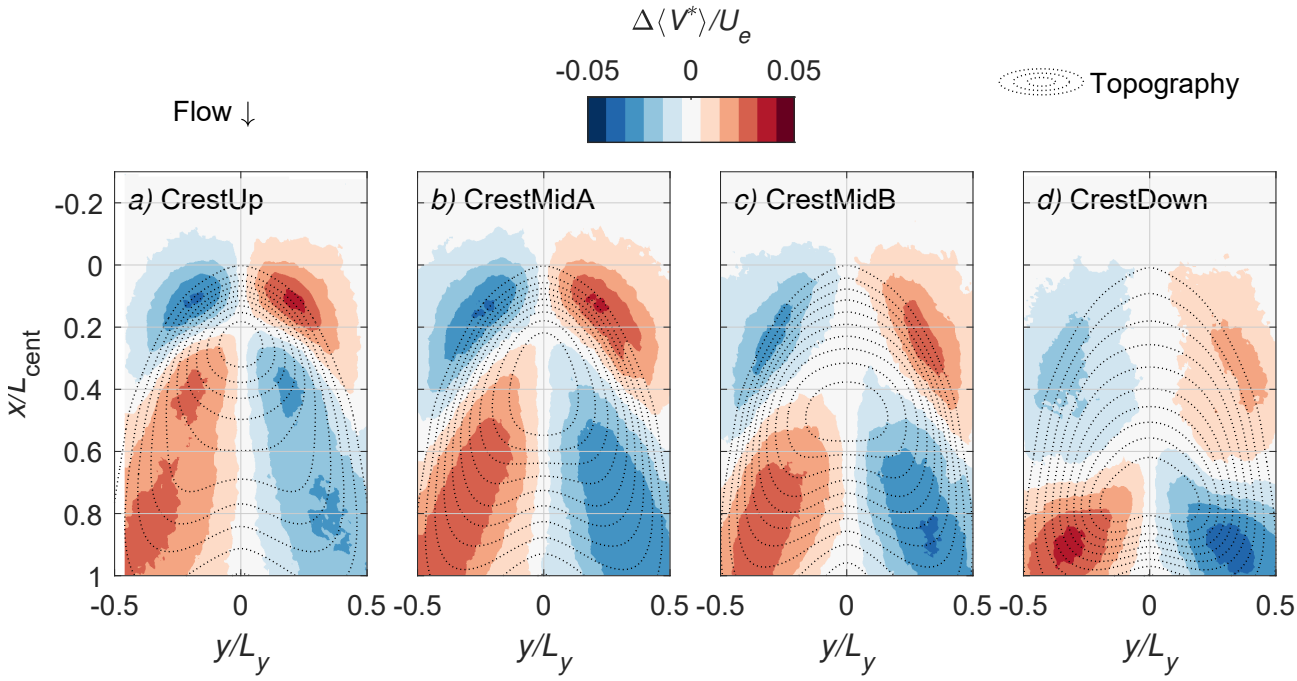

Figure 3: Disparity maps of $\langle V^* \rangle$ along x–y plane aligned with the crest height ($z/H = 1$). Dotted outlines overlaid shows underlying topographies.

same trend is reflected in the wall–parallel plots in Fig. 3, suggesting that the data in those plots, despite being a taken at the $z/H = 1$ above the wall, are remain good indicators of the conditions near the surface as well.

5. Reynolds normal stress v^2 from x–y plane

The difference between $\Delta\langle u^2 \rangle$ and $\Delta\langle v^2 \rangle$ in terms of phase-alignment with $\Delta\langle U \rangle$ is small, but evident in the same manner as for $\Delta\langle w^2 \rangle$ in the x–z plane where the relationship was most clear for the stoss side.

The magnitudes of the perturbations to $\langle u^2 \rangle$ and $\langle v^2 \rangle$ are not appreciably different, generally speaking, but their spatial distributions are different in the lee side of each protodune. In the lee sides, $\langle v^2 \rangle$ generally decreases relative to the incoming flow (i.e., negative disparity), whereas $\langle u^2 \rangle$ exhibits an increase beyond the crest for both CrestUp and CrestMidA. The decrease in $\langle v^2 \rangle$ in the wake is likely a result of the wake that the measurements are being

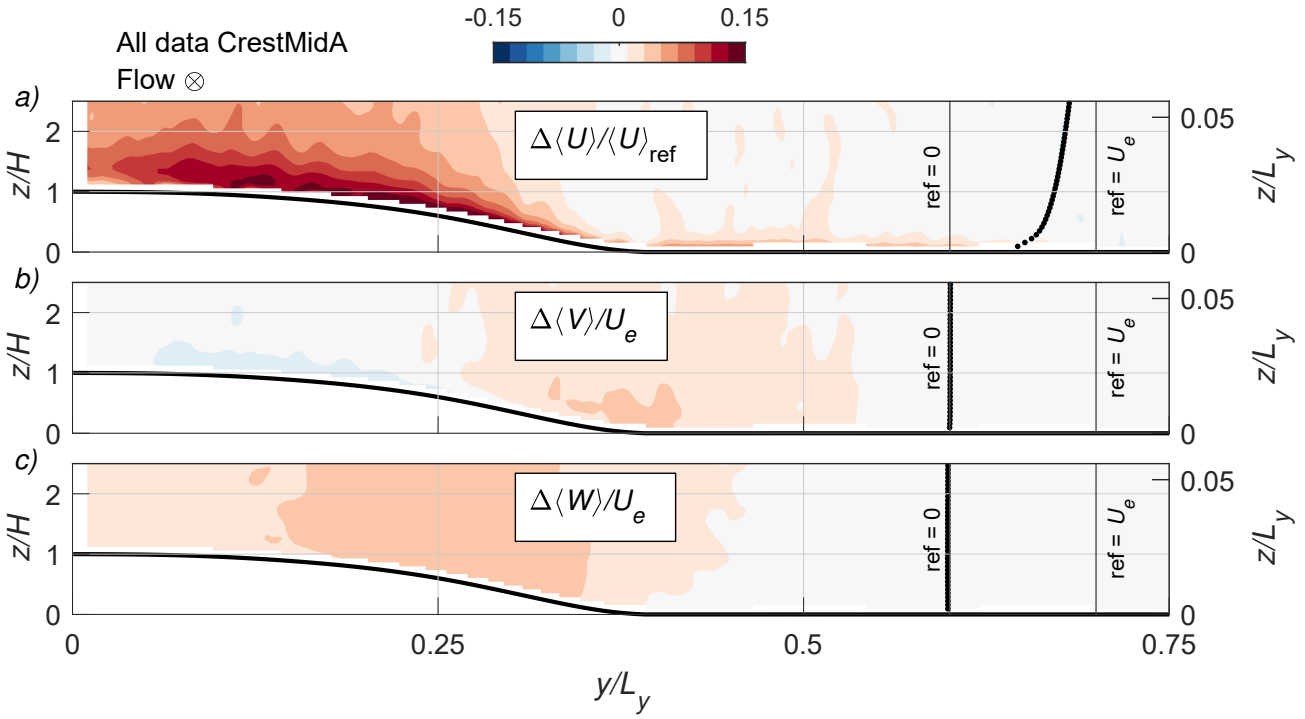

Figure 4: Cross-stream (y–z plane) disparity maps of mean velocities for CrestMidA case. Reference data from unperturbed region ($y/L_y \in [0.67, 0.75]$) used in calculating disparity is overlaid on right-hand-side with scale shown. Measurement plane is located at $x = 0.34L_{\mathrm{cent}} = 12.6H$, near the middle of the flat crest. Note that the bulk flow is directed out of the page. L_y is the full width of the entire bedform.

made above the region primarily increased turbulence. Looking at the perturbations of $\langle u^2 \rangle$ and $\langle w^2 \rangle$ from the x–z plane, it is clear that the increase in the Reynolds stresses is concentrated near the surface in the lee side, and is more confined for $\langle w^2 \rangle$ than for $\langle w^2 \rangle$. Due to the three-dimensionality of the topography, $\langle v^2 \rangle$ is expected to be relatively similar to $\langle w^2 \rangle$, which would explain the trends from measurements in this x–y plane aligned with the crest height.

6. Logarithmic mean velocity profiles

The incoming boundary layer, regardless of the dune placed downstream, is turbulent with an inner and outer layer structure. The overlapping region between the two layers has a logarithmic scaling for $\langle U(z) \rangle$ when normalized appropriately in viscous wall units, and hence why this is commonly referred to as the “log layer”. Viscous units are defined by normalization

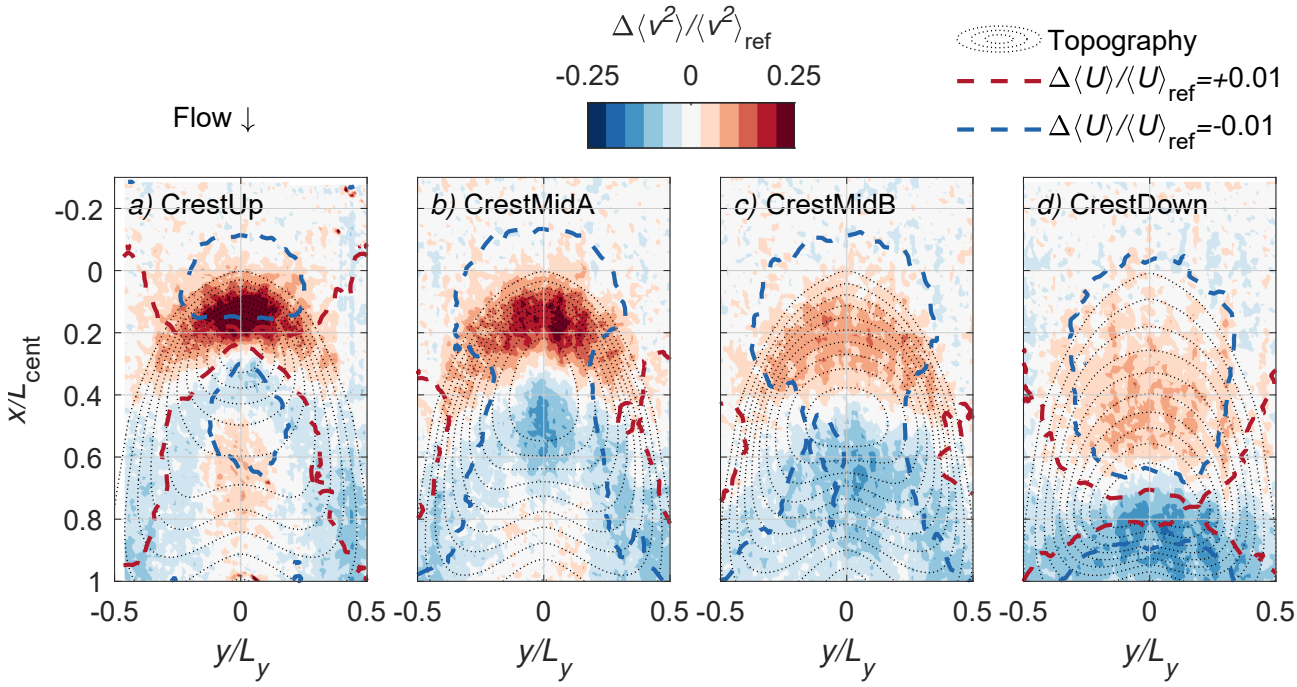

Figure 5: Disparity maps of $\langle v^2 \rangle$ along x–y plane aligned with crest ($z/H = 1$). Gray dotted profile overlaid upstream shows underlying topography. Blue and red dotted contour lines are overlaid to show coincident disparity of $\langle U \rangle$.

with friction velocity $u_\star$ and kinematic viscosity, ν, and are denoted by the $+$ superscript (i.e., $u^+ = u/u_\star$, $z^+ = zu_\star/\nu$). Since the friction velocity is merely a velocity scale defined by the mean wall shear stress, $\tau_0 = \rho u_\star^2$, this means that fitting the mean velocity profile to a logarithmic slope in the appropriate region (typically $z^+ > 30$, $z/\delta < 0.2$) will yield $u_\star$ and, by extension, τ_0. This logarithmic scaling of the mean velocity profile results from dimensional arguments associated with properties of wall turbulence, wherein the mean velocity gradient should scale as $\mathrm{d}\langle U \rangle/\mathrm{d}z \sim u_\star/z$, yielding the universal "law-of-the-wall". In the viscous sublayer (for smooth walls) the result is a linear velocity profile, whereas farther from the wall in the overlap region, for high Re_τ, both $z^+ \ggg 1$ and $z/\delta \ll 1$ apply and the law-of-the-wall integrates to

$$\langle U \rangle^+ = \frac{1}{\kappa} \log(z^+) + B, \tag{7}$$

where $\kappa = 0.384$ is von Kárman's constant, and $B = 4.17$ (Chauhan et al., 2007; Chauhan et al., 2009). This form gives $\langle U \rangle^+$ as a function of distance from the wall in viscous units, but for geophysical flows is more commonly recast as

$$\langle U \rangle^+ = \frac{1}{\kappa} \log \left(\frac{z}{z_0} \right), \tag{8}$$

where z_0 is the aerodynamic roughness length giving the height at which the log law goes to zero. An important additional property of the log layer (or inertial region), is that it also features a region of constant shear stress at high Re, which, if scaled by the friction velocity, $u_\star$, is unity. The total shear stress in this region is almost entirely due to $\langle -uw \rangle$, which is therefore an additional proxy for determining the mean shear stress at the wall, assuming the boundary layer is in equilibrium. This assumption of equilibrium, however, can be broken when the flow is subjected to strong, or rapid, changes in pressure gradients or surface curvature that may result in the development of an internal boundary layer (Garratt, 1990). In this case, both the log-linearity of $\langle U(z) \rangle$ and the scaling of $\langle -uw \rangle$ with $u_\star$ to unity may no longer apply. Early studies of wind profiles over the stoss sides of aeolian dunes have noted such effects, wherein the velocity profiles are not log-linear due to flow acceleration near the surface, leading to poor performance of transport predictions based on fitted values of $u_\star$ (Mulligan, 1988; Frank and Kocurek, 1996). Similarly perturbed profiles over aeolian dunes have also been reported more recently by Weaver and Wiggs (2011) and Qian et al. (2021), and such non-linearity and the presence of single or multiple kinks in the velocity profile have been found in studies of flow over subaqueous dune roughness (Smith and McLean, 1977; McLean et al., 1999; McLean et al., 2008).

Mean velocity profiles over the dune models have been fitted at each streamwise grid position following the approach of Chauhan et al. (2007) and Chauhan et al. (2009) wherein the full boundary layer profile is utilized, and not only points in a presumed logarithmic region. Values of $\kappa = 0.384$ and $B = 4.17$ are used as prescribed therein, and values of $u_\star$ are output for each

profile. This approach leverages access to the whole flow field over the dune afforded by PIV measurements, as well as the ability to capture flow very near to the surface using RIM optics. Thus, fitting of the local value of $u_\star(x)$ was attempted for each streamwise position. It should be noted that in other disparity maps, where $u_\star$ is used for normalization, the value used therein was taken from the upstream, unperturbed turbulent boundary layer (i.e., $u_\star(-\infty)$).

7. Growth of an internal boundary layer

Precisely identifying the existence of an internal layer and quantifying its depth is, however, challenging. A common approach is to inspect sharp changes to the mean velocity profile and turbulent stresses that originate near the bed and propagate outwards (Antonia and Luxton, 1971; Webster et al., 1996; Jacobi and McKeon, 2011). This is demonstrated in Fig. 6a–d, where contours of $\langle u^2 \rangle$ are plotted and overlaid with chosen contours from $\Delta\langle u^2 \rangle / \langle u^2_{\text{ref}} \rangle$. For cases CrestUp and CrestMidA, kinks or so-called "knee points" (Antonia and Luxton, 1971) in the contours of $\langle u^2 \rangle$ are evident, approximately intersected by the solid line indicating negative disparity from the upstream boundary layer.

However, these "knee point" features do not provide a very quantitatively rigorous assessment, which complicates identification of the internal layer. Although these features are readily observed from contours of the relatively strong flow perturbation (e.g., CrestUp and CrestMidA), the picture is less clear for a weaker perturbation (e.g., CrestDown). Therefore, although the overlaid contours of $\Delta\langle u^2 \rangle / \langle u^2_{\text{ref}} \rangle$, which coincide with the knee points, could plausibly be taken as a measure of δ_i (the local internal boundary layer thickness), this should be interpreted with caution.

Comparing all cases against each other, δ_i appears to grow to a similar depth for all cases between the toe and crest, although CrestMidB and CrestDown have more noisy trends due to the weaker perturbations of $\langle u^2 \rangle$. Contrary to this trend, one might reasonably assume that since CrestUp generally perturbs the flow more strongly than CrestDown, their internal

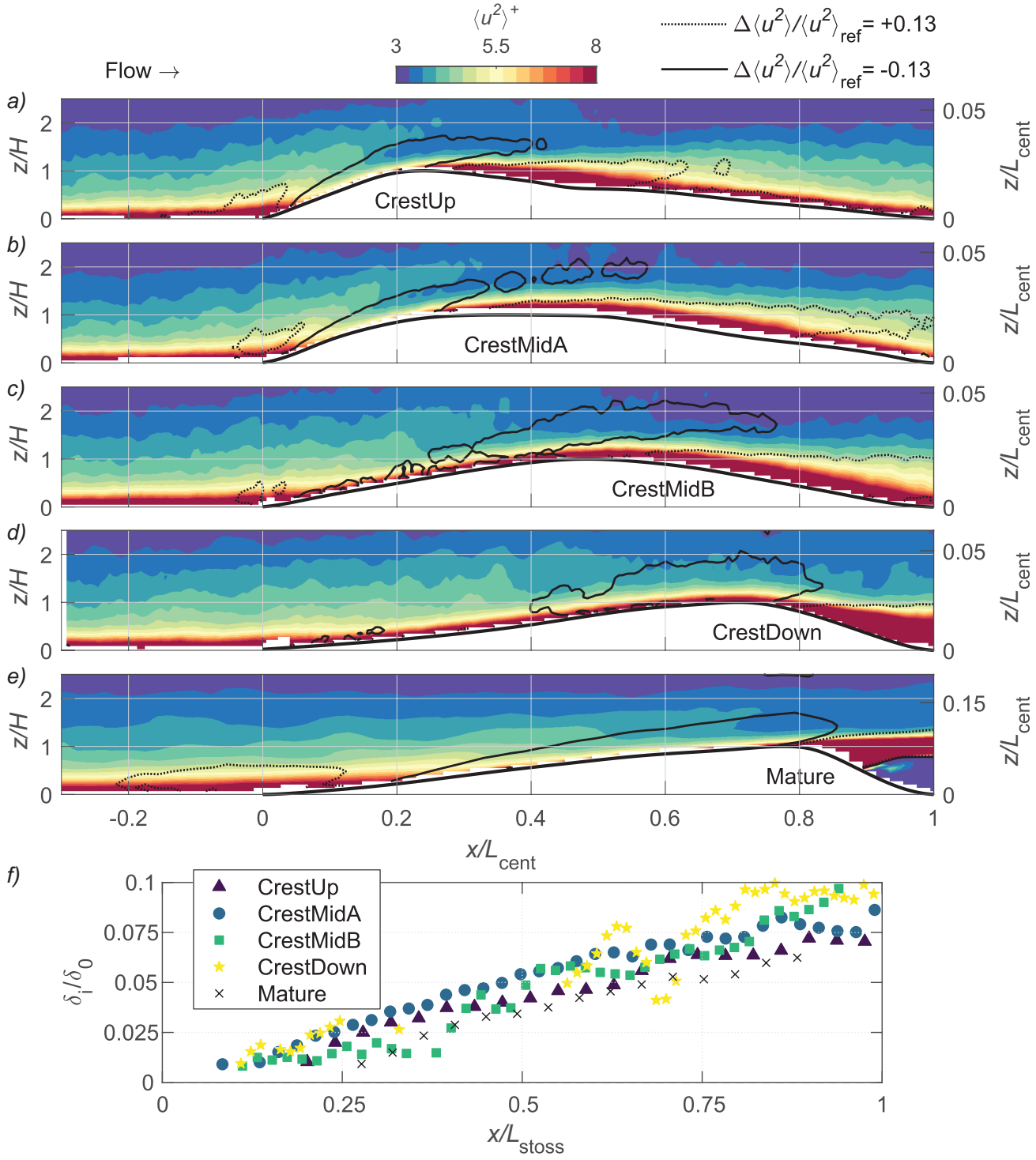

Figure 6: (a–d) Reynolds normal stress, $\langle u^2 \rangle^+$, overlaid with select contours of its disparity with unperturbed upstream data to highlight "knee points" in $\langle u^2 \rangle^+$ contours. (e) Internal boundary layer depth normalized by unperturbed boundary layer thickness, δ_0.

boundary layers should be distinguished in some way other than depth. In this sense, the differing degrees of reduction in $\langle -uw \rangle$ could be an important additional aspect of these internal layers.

8. Pressure gradient effects

The perturbation of the turbulent boundary layer by the protodune models can be understood in terms of pressure gradients and surface curvature (e.g., Taylor et al., 1987; Finnigan et al., 1990; Wiggs et al., 1996). Such effects have also been investigated in past studies of the aerodynamics of flow over gentle "bumps" (Webster et al., 1996) or models of hills (Finnigan et al., 1990), over both smooth and rough surfaces. Although pressure gradients and surface curvature can affect the flow in disparate ways, over the stoss side they are closely linked where the curving topography results in both a pressure gradient and curved streamlines. In particular, at the toe, the surface curvature is concave, and thus an adverse pressure gradient (APG) develops, where $\mathrm{d}p/\mathrm{d}x > 0$, and flow decelerates. Gradually over the stoss side, surface curvature changes from concave to convex, and the pressure gradient becomes favorable (FPG), where $\mathrm{d}p/\mathrm{d}x < 0$, resulting in flow acceleration. Immediately beyond the crest, curvature remains convex, but the orientation of the surface relative to the mean flow above results in an APG instead of an FPG, and thus the flow "expands" as it did over the toe.

In general, under the influence of an APG, the mean shear stress at the surface, τ_0, decreases. Such a trend was clearly evident for the fitted values of $u_\star(x)$, where in the decelerated region at the dune toe the values decrease, suggesting that the fitted values of $u_\star(x)$ are accurate, at least in their broad trends. Decreasing τ_0 under an APG can continue until eventually $\tau_0 = 0$ and the flow separates, at first intermittently as was the case for the wake of CrestDown, and if the pressure gradient is strong enough, flow separates more permanently as in the Mature case. This continuous flow separation in the lee side is a fundamental part of the dynamics of

mature bedforms with grainfall (Walker and Nickling, 2002; Baddock et al., 2011; Smith et al., 2017; Bristow et al., 2018). However, intermittent separation could also occur at the toe if the APG was strong enough there due to a steeper stoss slope. Indeed, such an APG drives the horseshoe vortex that forms upstream of a wall-mounted bluff body such as a cylindrical post or hemisphere (Simpson, 2001). Although flow separation is the extreme case of an APG, well before this occurs the flow becomes increasingly unstable near the surface, and the outer extent of the viscous sublayer lessens (Nickels, 2004). This increased unsteadiness in the flow is seen in the Reynolds stresses, where their disparity relative to the incoming flow is positive over the toe.

However, the increase in Reynolds stress is not the same for all components. Streamwise Reynolds normal stress, $\langle u^2 \rangle$, remains in-phase with $\Delta\langle U \rangle$, while $\langle w^2 \rangle$ and $\langle uw \rangle$ lag spatially. This is because, as shown by Finnigan et al. (1990) for hills and Wiggs et al. (1996), Weaver and Wiggs (2011), and Baddock et al. (2011) for mature dunes, $\langle u^2 \rangle$ follows flow acceleration, and thus pressure gradient, while $\langle uw \rangle$ and $\langle w^2 \rangle$ respond to streamline curvature. Thus, although the APG at the dune toe extends somewhat upstream, leading to a gradual flow deceleration approaching the toe along with an increase in $\langle u^2 \rangle$, streamline curvature does not develop until the toe itself is reached, when $\langle W \rangle$ becomes non-zero. Thereafter $\langle w^2 \rangle$ and $\langle uw \rangle$ both increase, before then decreasing mid-stoss as the surface curvature becomes negative (i.e., convex).

One key difference between the protodunes examined herein is that the surface curvature is significantly different among the cases, where the relatively short stoss slope of CrestUp and CrestMidA result in a stronger curvature, and CrestMidB and CrestDown are far more gentle in this regard. Thus, $\Delta\langle w^2 \rangle$ and $\Delta\langle uw \rangle$ are much larger in magnitude (both positive and negative) for CrestUp and CrestMidA. However, the flatter crest of CrestMidA results in the region of stronger convex curvature that precedes the crest being located farther upstream than that of CrestUp. In other words, CrestMidA more closely resembles a crest–brink separated mature

dune in its overall morphology, compared to CrestUp. This enables the speed-up to peak prior to the crest, and likewise for the fitted values of $u_\star(x)$ and minima in Reynolds stresses.

References

Antonia, R. A. and Luxton, R. E. (1971). The response of a turbulent boundary layer to a step change in surface roughness Part 1. Smooth to rough. *J. Fluid Mech.* 48 (4): 721–761.

Baars, W. J., Hutchins, N., and Marusic, I. (2017). Self-similarity of wall-attached turbulence in boundary layers. *J. Fluid Mech.* 823.

Baddock, M. C., Wiggs, G. F. S., and Livingstone, I. (2011). A field study of mean and turbulent flow characteristics upwind, over and downwind of barchan dunes. *Earth Surf. Process. Landforms* 36 (11): 1435–1448.

Bristow, N. R., Blois, G., Best, J. L., and Christensen, K. T. (2018). Turbulent flow structure associated with collision between laterally offset, fixed-bed barchan dunes. *J. Geophys. Res. Earth Surf.* 123 (9): 2157–2188.

Chauhan, K. A., Hutchins, N., Monty, J., and Marusic, I. (2013). Structure inclination angles in the convective atmospheric surface layer. *Bound. Layer Meteorol.* 147 (1): 41–50.

Chauhan, K. A., Monkewitz, P. A., and Nagib, H. M. (2009). Criteria for assessing experiments in zero pressure gradient boundary layers. *Fluid Dyn. Res.* 41 (2): 21404.

Chauhan, K. A., Nagib, H., and Monkewitz, P. (2007). On the composite logarithmic profile in zero pressure gradient turbulent boundary layers. In: *45th AIAA Aerosp. Sci. Meet. Exhib.* 532.

Claudin, P., Wiggs, G. F. S., and Andreotti, B. (2013). Field evidence for the upwind velocity shift at the crest of low dunes. *Boundary-Layer Meteorol.* 148 (1): 195–206.

Del Álamo, J. C., Jimenez, J., Zandonade, P., and Moser, R. D. (2006). Self-similar vortex clusters in the turbulent logarithmic region. *J. Fluid Mech.* 561: 329–358.

247 Finnigan, J. J., Raupach, M. R., Bradley, E. F., and Aldis, G. K. (1990). A wind tunnel study
248 of turbulent flow of over a two-dimensional ridge. *Boundary-Layer Meteorol.* 50 (1-4): 277–
249 317.
250 Frank, A. J. and Kocurek, G. (1996). Airflow up the stoss slope of sand dunes: limitations of
251 current understanding. *Geomorphology* 17 (1-3): 47–54.
252 Ganapathisubramani, B., Hutchins, N., Hambleton, W. T., Longmire, E. K., and Marusic, I.
253 (2005). Investigation of large-scale coherence in a turbulent boundary layer using two-point
254 correlations. *J. Fluid Mech.* 524: 57–80.
255 Garratt, J. R. (1990). The internal boundary layer—A review. *Boundary-Layer Meteorol.* 50
256 (1): 171–203.
257 Hommema, S. E. and Adrian, R. J. (2003). Packet structure of surface eddies in the atmo-
258 spheric boundary layer. *Boundary-Layer Meteorol.* 106 (1): 147–170.
259 Hutchins, N., Hambleton, W. T., and Marusic, I. (2005). Inclined cross-stream stereo particle
260 image velocimetry measurements in turbulent boundary layers. *J. Fluid Mech.* 541: 21–54.
261 Hutchins, N., Chauhan, K., Marusic, I., Monty, J., and Klewicki, J. (2012). Towards reconciling
262 the large-scale structure of turbulent boundary layers in the atmosphere and laboratory.
263 *Boundary-Layer Meteorol.* 145 (2): 273–306.
264 Jacobi, I. and McKeon, B. J. (2011). New perspectives on the impulsive roughness-perturbation
265 of a turbulent boundary layer. *J. Fluid Mech.* 677: 179–203.
266 Krug, D., Baars, W. J., Hutchins, N., and Marusic, I. (2019). Vertical coherence of turbulence
267 in the atmospheric surface layer: connecting the hypotheses of Townsend and Davenport.
268 *Boundary-Layer Meteorol.* 172 (2): 199–214.
269 Marusic, I. and Monty, J. P. (2019). Attached eddy model of wall turbulence. *Annu. Rev. Fluid*
270 *Mech.* 51: 49–74.
271 Marusic, I., Monty, J. P., Hultmark, M., and Smits, A. J. (2013). On the logarithmic region in
272 wall turbulence. *J. Fluid Mech.* 716: R3.

McLean, S. R., Wolfe, S. R., and Nelson, J. M. (1999). Spatially averaged flow over a wavy boundary revisited. *J. Geophys. Res. Ocean.* 104 (C7): 15743–15753.

McLean, S. R., Nikora, V. I., and Coleman, S. E. (2008). Double-averaged velocity profiles over fixed dune shapes. *Acta Geophys.* 56 (3): 669.

Morris, S. C., Stolpa, S. R., Slaboch, P. E., and Klewicki, J. C. (2007). Near-surface particle image velocimetry measurements in a transitionally rough-wall atmospheric boundary layer. *J. Fluid Mech.* 580: 319–338.

Mulligan, K. R. (1988). Velocity profiles measured on the windward slope of a transverse dune. *Earth Surf. Process. Landforms* 13 (7): 573–582.

Nickels, T. B. (2004). Inner scaling for wall-bounded flows subject to large pressure gradients. *J. Fluid Mech.* 521: 217.

Qian, G., Yang, Z., Tian, M., Dong, Z., Liang, A., and Xing, X. (2021). From dome dune to barchan dune: Airflow structure changes measured with particle image velocimetry in a wind tunnel. *Geomorphology*: 107681.

Salesky, S. T. and Anderson, W. (2018). Buoyancy effects on large-scale motions in convective atmospheric boundary layers: implications for modulation of near-wall processes. *J. Fluid Mech.* 856: 135–168.

Simpson, R. L. (2001). Junction flows. *Annual Review of Fluid Mechanics* 33 (1): 415–443.

Smith, A. B., Jackson, D. W. T., and Cooper, J. A. G. (2017). Three-dimensional airflow and sediment transport patterns over barchan dunes. *Geomorphology* 278: 28–42.

Smith, J. D. and McLean, S. R. (1977). Spatially averaged flow over a wavy surface. *J. Geophys. Res.* 82 (12): 1735–1746.

Taylor, P. A., Mason, P. J., and Bradley, E. F. (1987). Boundary-layer flow over low hills. *Boundary-Layer Meteorol.* 39 (1-2): 107–132.

Tomkins, C. D. and Adrian, R. J. (2003). Spanwise structure and scale growth in turbulent boundary layers. *J. Fluid Mech.* 490: 37–74.

Townsend, A. A. R. (1976). The structure of turbulent shear flow. Cambridge University Press.

300 Walker, I. J. and Nickling, W. G. (2002). Dynamics of secondary airflow and sediment transport
301 over and in the lee of transverse dunes. *Prog. Phys. Geogr.* 26 (1): 47–75.
302 Wang, G. and Zheng, X. (2016). Very large scale motions in the atmospheric surface layer: a
303 field investigation. *J. Fluid Mech.* 802: 464–489.
304 Weaver, C. M. and Wiggs, G. F. S. (2011). Field measurements of mean and turbulent airflow
305 over a barchan sand dune. *Geomorphology* 128 (1-2): 32–41.
306 Webster, D. R., DeGraaff, D. B., and Eaton, J. K. (1996). Turbulence characteristics of a
307 boundary layer over a swept bump. *J. Fluid Mech.* 323: 1–22.
308 Wiggs, G. F. S., Livingstone, I., and Warren, A. (1996). The role of streamline curvature in
309 sand dune dynamics: evidence from field and wind tunnel measurements. *Geomorphology*
310 17 (1-3): 29–46.